Enhancing Demodulation Performance of DCM Algorithm in φ-OTDR System Through Temporal Spline Interpolation

Tingyu WANG[1], Jianzhong ZHANG[1*], Zhe MA[2*], Xiang HE[1], Weizhe LI[1], Binyuan YANG[1], and Mingjiang ZHANG[1,3,4]

[1]*Key Laboratory of Advanced Transducers and Intelligent Control Systems (Ministry of Education and Shanxi Province), Taiyuan University of Technology, Taiyuan 030024, China*

[2]*College of Electronic Information and Optical Engineering, Taiyuan University of Technology, Taiyuan 030024, China*

[3]*College of Physics, Taiyuan University of Technology, Taiyuan 030024, China*

[4]*Shanxi-Zheda Institute of Advanced Materials and Chemical Engineering, Taiyuan 030024, China*

[*]Corresponding authors: Jianzhong ZHANG and Zhe MA E-mail: zhangjianzhong@tyut.edu.cn and mazhe@tyut.edu.cn

Abstract: For expanding the amplitude-frequency response range of the differential cross-phase multiply (DCM) algorithm in the φ-OTDR system, a temporal spline interpolation (TSI) method is proposed to pre-process Rayleigh backscattering (RBS) signals. Through the TSI method, the discrete temporal signals characterizing RBS traces are subjected to interpolation, facilitating a reduction in differential approximation errors. This, in turn, establishes a heightened level of precision in phase demodulation, especially relevant across extensive sensing distances. By comparing the recovered time-domain waveforms and the corresponding power spectral densities without and with the TSI, the above improvement effect has been experimentally validated by utilizing the TSI. The results show that, with the TSI, the amplitude-frequency response range of the DCM algorithm is enlarged by 2.78 times, and the new relationship among f_{pulse}, f, and D under the root mean square error (RMSE) tolerance less than 0.1 can be expressed as $1.9(D+1)f \le f_{\text{pulse}}$. This contribution underscores a substantial advancement in the capabilities of the DCM algorithm, holding promise for refined performance in optical fiber sensing applications.

Keywords: φ-OTDR; DCM algorithm; phase demodulation; 3×3 coupler; temporal spline interpolation

Citation: Tingyu WANG, Jianzhong ZHANG, Zhe MA, Xiang HE, Weizhe LI, Binyuan YANG, *et al.*, "Enhancing Demodulation Performance of DCM Algorithm in φ-OTDR System Through Temporal Spline Interpolation," *Photonic Sensors*, 2024, 14(3): 240308.

1. Introduction

Recently, the phase-sensitive optical time-domain reflectometer (φ-OTDR) has been successfully applied in the monitoring of the seismic wave [1–3], traffic flow [4], and pipeline integrity [5], etc., due to its advantages of distributed sensing, sensitivity to vibration, and resistance to electromagnetic interference. In a φ-OTDR system, phase demodulation plays a crucial role as it transfers measured Rayleigh backscattering (RBS) signals to target vibration information, i.e., the frequency, amplitude, and initial phase of the vibration signal [6]. There are many phase demodulation techniques, including digital coherent demodulation [7–9], phase generation carrier (PGC)

Received: 22 September 2023 / Revised: 12 January 2024

DOI: 10.1007/s13320-024-0725-1
Article type: Regular

[10, 11], and 3×3 coupler demodulation [12–28], among which the 3×3 coupler demodulation technique has been increasingly favored by researchers because it does not require additional carrier modulation and exhibits higher robustness against interference fading [12].

The most commonly used demodulation algorithms for the 3×3 coupler demodulation system are the Arctan [13, 14] and the differential cross-phase multiply (DCM) algorithms [15–28]. Compared with the Arctan algorithm, the DCM algorithm has a simpler calculation process and can avoid phase unwrapping [29], making it easier to use in practical applications. For example, the DCM phase demodulation algorithm in combination with pattern recognition has been performed in pipeline protection, human locomotion classification, soil moisture content monitoring, etc. [23–27]. Various improvement methods have been proposed for the DCM-based 3×3 coupler demodulation process to enhance its demodulation performance. For instance, by introducing an interferometer to the 3×3 coupler demodulation system, i.e., the Mach-Zender interferometer (MZI) [15], or Michelson interferometer (MI) [16–19], the higher sensitivity, better signal-to-noise ratio (SNR), and larger demodulated signal width were offered. Through a combination of a low-noise laser, a high-gain erbium-doped fiber amplifier and other optimized optical components, a sensing distance of 40 km was achieved in the 3×3 coupler demodulation system [20]. By employing ultra-weak fiber Bragg gratings, the performance of the φ-OTDR system with 3×3 coupler demodulation was enhanced [17, 21]. An improved two-path DCM algorithm was proposed to reduce system hardware costs and minimize the impact of incomplete symmetry of the 3×3 coupler [22]. Although the above improvement measures can be applied to the long-distance application, the differential operation in the DCM algorithm still causes the phase retrieval more prone to noise [28, 30], thus limiting the practical applications of this algorithm.

To maintain a high level of precision in DCM phase demodulation, it is necessary to reduce the differential approximation errors. With this goal, we propose a data pre-processing method before demodulation using temporal spline interpolation (TSI). This method enables nonlinear interpolation of the temporal signals characterizing the RBS traces at each position along the fiber. Subsequently, the vibration phase can be obtained by demodulating the interpolated data with the DCM algorithm. Compared with the original demodulation results, the TSI method significantly reduces phase errors and greatly expands the amplitude-frequency response range. Moreover, it does not need any hardware modification in an existing sensing system and can be adopted by a 3×3 coupler demodulation system based on the DCM algorithm.

2. Experimental setup and principle

2.1 Experimental Setup

A φ-OTDR system with 3×3 coupler demodulation is built to investigate whether the TSI can enhance the demodulation performance of the DCM algorithm. The whole experimental setup is illustrated in Fig. 1. The light source consists of a fiber laser with a wavelength of 1 550.12 nm and a linewidth lower than 3 kHz, ensuring a long coherent length. The continuous light emitted from the laser is modulated into a sequence of optical pulses by an acousto-optic modulator (AOM) with an SNR higher than 50 dB and a rise time less than 10 ns. The parameters of the pulse, i.e., the pulse width of 100 ns, and the pulse repetition frequency (f_{pulse}) of 12 500 Hz, are set through the data acquisition module (DAQ), where electrical pulses are generated and converted into radio frequency (RF) signals by the AOM driver (AOMD). The resulting optical pulses are injected into a single-mode fiber (SMF) through a circulator (Cir1), in which process, the RBS light is excited due to the

photoelastic effect. Then, the RBS light enters the phase demodulation module through the same circulator Cir1. The optical pulse and RBS light are separately amplified by erbium-doped fiber amplifiers (EDFA1 and EDFA2) and the amplified RBS light is filtered in a filter with a bandwidth of 0.1 nm to suppress amplified spontaneous emission noise.

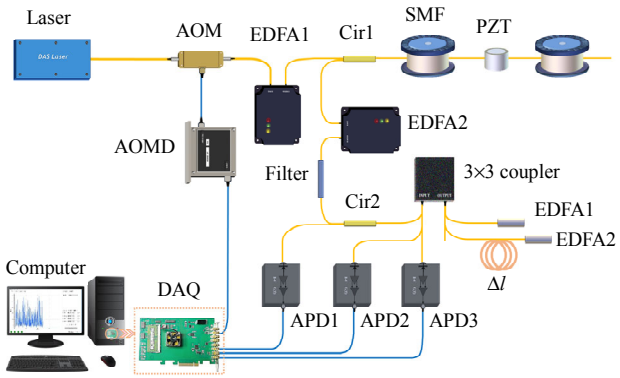

Fig. 1 Diagram of the experimental setup.

The phase demodulation module consists of Cir2, the 3×3 coupler, and the MI that enhances the sensitivity of the system. The interference arms of the MI are connected to two Faraday rotating mirrors (FRMs) and have a path difference Δl of 5 m. The transmission process of RBS light in the phase demodulation module is as follows: 1) the RBS light is injected into the 3×3 coupler through Cir2 and divided into three beams; 2) two of these beams enter the interferometer arms of the MI and are reflected by the FRMs; 3) the reflected light converges and interferes in the 3×3 coupler, resulting in three beams that have a relative phase difference of 120°. The three beams of light are converted by the avalanche photodetectors (APD1, APD2, and APD3) into electrical signals, which are sampled by the DAQ with a sampling rate of 250 MSa/s and quantization bit depth of 14 bits, and then, the discrete sampled signals are transmitted to a computer for further phase demodulation processing.

In the experiment, the vibration events are generated by employing a piezoelectric transducer (PZT), which is placed at the position of about 2 590 m of the SMF, with a fiber stretching length of 10 m.

2.2 Principle

In this section, we first introduce the principle of 3×3 coupler demodulation in the φ-OTDR system, and then we will explain the improvement mechanism of the proposed TSI method for the DCM algorithm.

As shown in Fig. 2(a), in the φ-OTDR system, during the traveling of a high-coherent pulse along the sensing fiber, the RBS light is excited due to the photoelastic effect. The RBS light, which contains the environmental information, is then transferred into RBS signals through photoelectric conversion and DAQ sampling. In demodulation, the collected RBS signals are reconstructed as a two-dimensional (2-D) matrix, i.e., the spatial signals along the "sensing distance" axis and the temporal signals along the "response time" axis. The spatial signals are obtained through the synthesis of coherent superposition of RBS light within a half-pulse width. Note that the spatial signals within a pulse duration are referred to as an RBS trace. On the other hand, the temporal signal characterizes the intensity variations of the RBS trace at a specific position, and its temporal sampling rate corresponds to the pulse repetition frequency (f_{pulse}). When a vibration event occurs and acts on the sensing fiber, the intensities of the spatial signals are stochastic, while fluctuations are observed in the intensity of the temporal signal at that specific position. By analyzing these fluctuations, the vibration information can be recovered.

The phase demodulation module with a 3×3 coupler can output three-channel temporal signals with a relative phase difference of 120°. Assuming that the 3×3 coupler is symmetric and the vibration event is a single-frequency signal, the three output temporal signals I_m collected at the position z and time t_s can be described as

$$I_m(t_s) = B_z + A_z \cos\left[\phi(t_s) + (m-1)\cdot\frac{2\pi}{3}\right],\ m = 1, 2, 3 \quad (1)$$

where m is the serial number of the output channel, B_z and A_z are the direct current (DC) part and alternating current (AC) part of $I_m(t_s)$, respectively, t_s is the time in the "response time" axis, $\Delta t_s = 1/f_{\text{pulse}}$ is the time interval dependent on the time delay of the pulse emission, and $\phi(t_s)$ is the phase of the vibration-event-modulated temporal signal and is expressed as

$$\phi(t_s) = D\cos(2\pi f t_s + \varphi) \quad (2)$$

where D is the vibration amplitude, f is the vibration frequency, and φ is the initial phase.

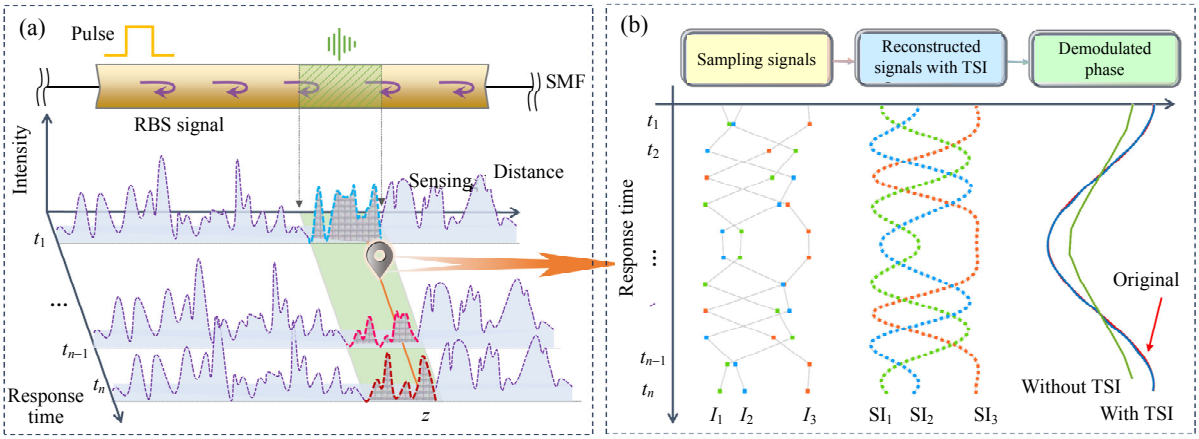

Fig. 2 Schematic diagram of (a) 3×3 coupler demodulation in the φ-OTDR system and (b) improvement mechanism of the proposed TSI method for the DCM algorithm.

In the traditional calculation process of the DCM demodulation algorithm, the phase $\phi(t_s)$ of the $I_m(t_s)$ is extracted by sequentially performing the following operations: elimination of DC, differentiation, cross-multiplication, and integration [30]. It is worth noting that considering the discreteness of $I_m(t_s)$, we use the first-order forward finite difference method to approximate the differential values. This differential approximate method is easily implemented on the computer [31].

According to the Taylor expansion definition, the differential approximation error $\delta_{I_m}(t_s)$ can be written as

$$\delta_{I_m}(t_s) = -\frac{I_m''(t_s)}{2}\Delta t_s + O(\Delta t_s^2) \quad (3)$$

where $I_m''(t_s)$ is the second-order derivative of the signal acquired from the mth channel, and this value increases with an increase in D and f; $O(\Delta t_s^2)$ is a small term that can be neglected. The error $\delta_{I_m}(t_s)$ will propagate through the calculation process of the DCM algorithm and result in demodulated phase errors.

The amplitude of error $\delta_{I_m}(t_s)$ is mainly affected by f, D, and f_{pulse}. To reduce the error, we can increase f_{pulse}, however, this value is limited by the fiber length L, according to the inequality $f_{\text{pulse}} \leq c/(2n_f L)$, where c is the speed of light in vacuum, n_f is the effective refractive index of the fiber. This constraint implies that there is a theoretical limit for error reduction by adjusting f_{pulse}. For long-distance vibration sensing, L is large and thus f_{pulse} is smaller. As a result, only vibration signals with smaller f and D can be well demodulated, and in other words, the amplitude-frequency response range of the DCM algorithm is narrowed. This limitation restricts the practical application of the DCM algorithm.

To address the above problem, we introduce a pre-processing method using the TSI method before demodulation. The calculation principle of the TSI can be found in [32]. Figure 2(b) shows the schematic diagram of the improved phase demodulation process. Specifically, the TSI performs a nonlinear fitting on the waveform of the

temporal signals I_m, giving a series of cubic spline functions. Then, these functions are used to interpolate the signal I_m, and the interpolated result is denoted as SI_m. The SI_m is the input signal for the DCM algorithm to obtain a demodulated phase. As shown in Fig. 2(b), the phase obtained with the TSI matches well with the original phase, while the demodulated phase without the TSI is significantly distorted. The reason why the TSI enhances the demodulation performance of DCM is that it "narrows down" the time interval Δt_s by increasing the number of sampling points per unit time according to the fitted cubic spline function. As a result, the differential approximation errors $\delta_{I_m}(t_s)$ are reduced, leading to a decrease in the final demodulation phase errors.

The normalized root mean square error (RMSE) is used to quantitatively describe the phase demodulation error, which can be expressed as follows:

$$\mathrm{RMSE}=\sqrt{\frac{1}{n}\sum_{i=1}^{n}\left(\frac{Y_i-y_i}{D}\right)^2} \tag{4}$$

where n is the total sampling number in calculation, and Y_i and y_i are the values of the original and demodulated phases of the ith sampling point, respectively.

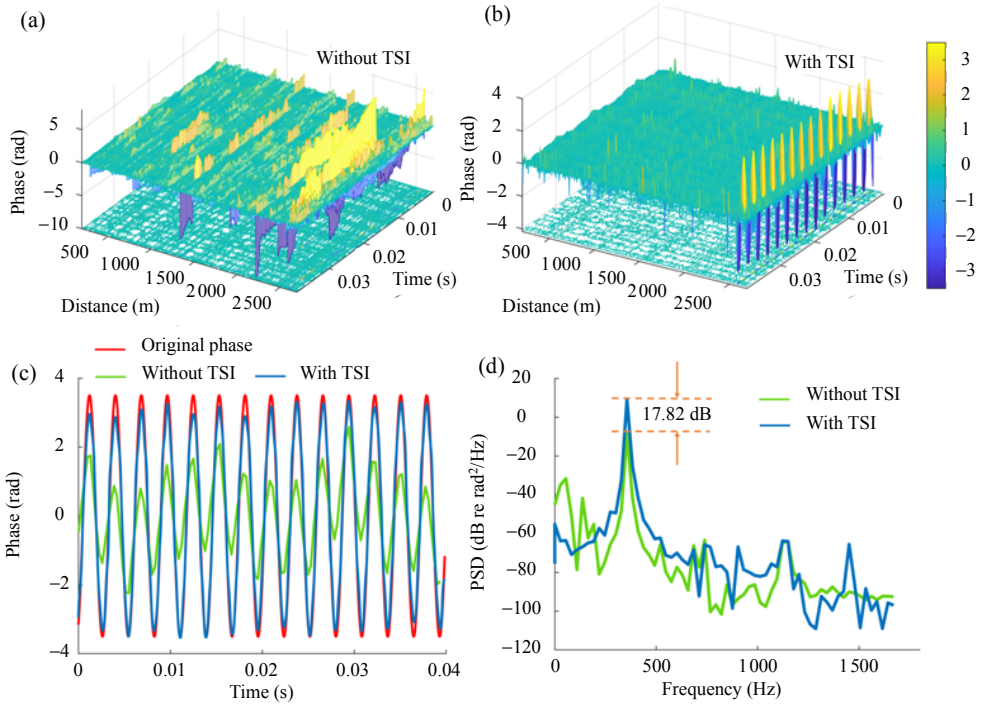

Fig. 3 Spatial-temporal maps of the demodulated phase: (a) without the TSI, (b) with the TSI, (c) extracted phase time-domain waveforms at 2 588 m, and (d) PSD curves.

3. Experimental results and discussion

To verify the improvement capability of the TSI to the DCM algorithm, we compare the time-domain waveforms and power spectral densities (PSD) of the demodulated phase without and with the TSI. In the experiment, a vibration signal is loaded by the PZT with the driving function being a sine wave with the frequency f at 357 Hz and a driving voltage V_{PZT} at 1 V (corresponding to D=3.5 rad). The number of sampling points for each vibration period is set to 9 to facilitate comparison of the demodulation phase changes without and with the TSI. Figures 3(a) and 3(b) show the spatial-temporal

maps of the demodulated phase obtained through the DCM algorithm without and with the TSI, respectively. Without the TSI, phase errors are observed in many positions along the sensing fiber, as demonstrated by the large changes in Fig. 3(a). These positions cannot be distinguished from the actual vibration position (approximately 2 590 m), leading to false alarms. The above phenomenon can be attributed to the existence of differential approximation error. Additionally, the noises caused by the environmental perturbations and photodetection also affect the differentiation results [28]. The above errors propagate during the calculation process of the DCM algorithm, eventually resulting in severe phase distortion. In contrast, by applying the TSI, the demodulated phase well reflects the full vibration information and the false alarms are significantly reduced [Fig. 3(b)].

We extract the time-domain waveforms of the demodulated phase at 2 588 m for both cases without and with the TSI. These waveforms are then compared with the original phase, as illustrated in Fig. 3(c). It is evident that the demodulated phase obtained with the TSI closely matches the original phase, while significant amplitude distortion is observed when the TSI is not used. Additionally, we compare the corresponding PSD values, as shown in Fig. 3(d). The results indicate that by using the TSI, the low-frequency noises in the range of 0 Hz–200 Hz are effectively suppressed, and the PSD peak value at 357 Hz is increased by 17.82 dB. The above improvement can be explained by the smoothing effect of the cubic spline function on the noised signal [33].

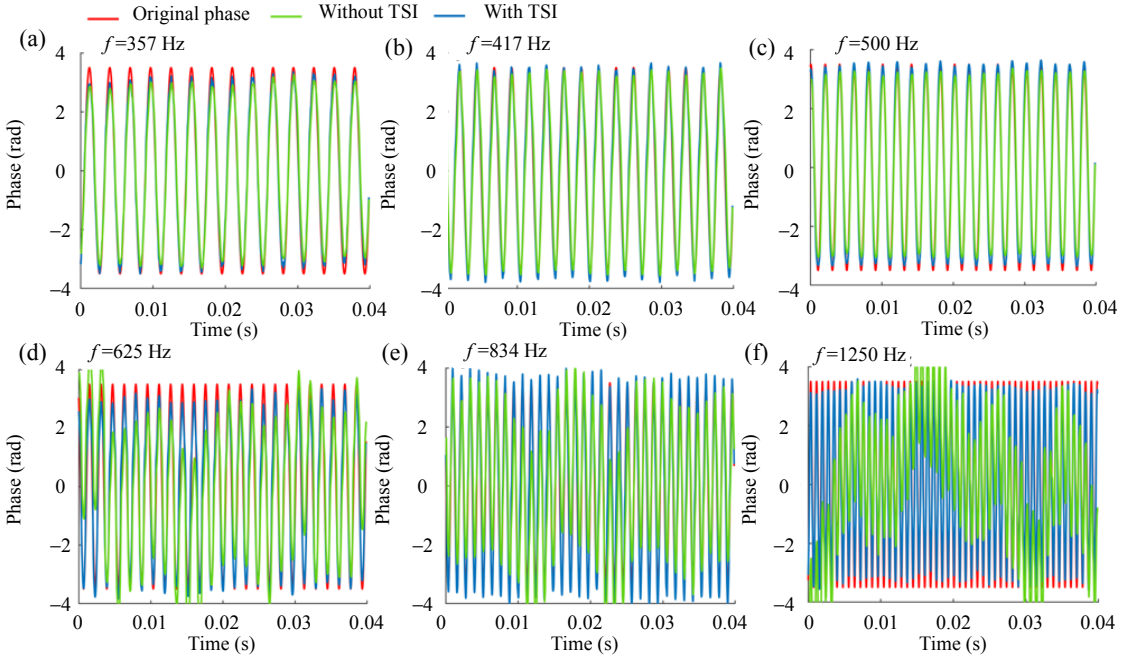

Fig. 4 Comparison of the time-domain phase waveforms obtained without and with the TSI at different vibration frequencies f: (a) 357 Hz, (b) 417 Hz, (c) 500 Hz, (d) 625 Hz, (e) 834 Hz, and (f) 1 250 Hz.

To investigate the effect of the TSI on the frequency response range of the DCM algorithm, at different vibration frequencies f, we compare the time-domain waveforms and PSD values of the demodulated phase with and without the TSI. In this experiment, the f_{pulse} and the driving voltage V_{PZT} are fixed at 12 500 Hz and 1 V, respectively. The vibration frequencies f are set to 357 Hz, 417 Hz, 500 Hz, 625 Hz, 834 Hz, and 1 250 Hz, respectively. Based on the above settings, the ratios f_{pulse}/f are 35, 30, 25, 20, 15, and 10, respectively, showing a decrease in the number of sampling points per

vibration period. Figures 4(a)–4(f) present the time-domain waveforms of the demodulated phase obtained at different vibration frequencies. Although the environmental disturbances around the fiber and the asymmetry of the 3×3 coupler (including the splitting ratio and phase difference) lead to under-response or over-response in the amplitude of the demodulated phase, it can still be seen that for vibration signals at 357 Hz and 417 Hz, whether or not the TSI is used, the demodulated phases match well with the original phase. However, as the vibration frequency f continuously increases, the quality of the time-domain waveforms without the TSI deteriorated. This deterioration is mainly characterized by distortion and random fluctuations of the amplitude. In contrast, when the TSI is applied, the demodulated phase shows a better alignment with the original phase, even for the vibration frequency f as high as 1 250 Hz.

Figure 5(a) shows a comparison of PSD curves obtained without and with the TSI at various vibration frequencies f. It can be observed that whether or not the TSI is used, the vibration frequencies ranging from 357 Hz to 1 250 Hz are able to be identified according to the PSD peaks. However, it is noteworthy that for the case without the TSI, as the vibration frequency f increases, the PSD values in the frequency range of 0 Hz–200 Hz increase, which suggests a rise in low-frequency noise components. When the vibration frequency f is as high as 1 250 Hz, the noise predominates the output phase: the PSD value is –5.40 dB re rad^2/Hz at 1 250 Hz, smaller than the value at 100 Hz (–4.83 dB re rad^2/Hz). When the TSI is applied, the low-frequency noise is significantly suppressed, with all PSD values of the low-frequency noise component below –62 dB re rad^2/Hz. Furthermore, the PSD peak values corresponding to different vibration frequencies f are compared between the cases without and with the TSI, and a bar chart is plotted as shown in Fig. 5(b). The comparison results show that, when the TSI is used, the PSD value of different f is increased by 1.25 dB, 1.59 dB, 2.26 dB, 3.36 dB, and 7.05 dB, respectively. Especially for the vibration frequencies f at 834 Hz and 1 250 Hz, the improvement of phase demodulation quality is more significant.

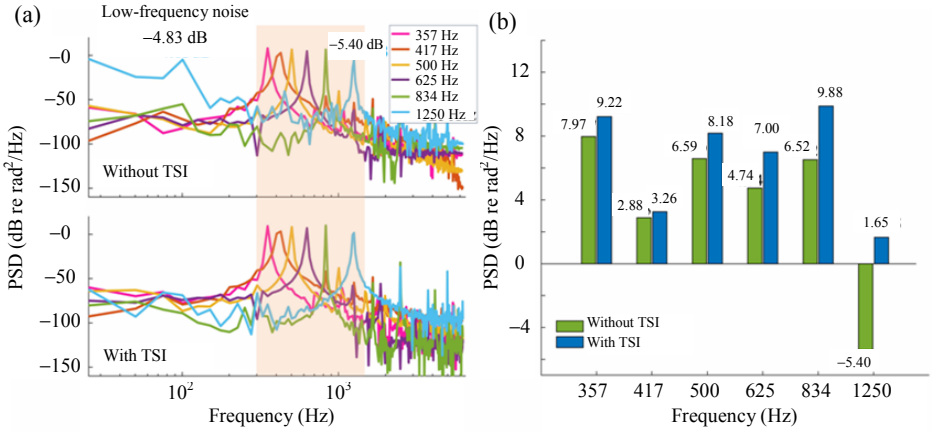

Fig. 5 Comparison of (a) the PSD curves and (b) their PSD peak values obtained without and with the TSI at various vibration frequencies f.

The effect of the TSI on the amplitude response range of the DCM algorithm is also investigated. At different voltages V_{PZT}, we compare the time-domain waveforms acquired without and with the TSI, as shown in Figs. 6(a)–6(e). In the experiment, the ratio f_{pulse}/f is fixed at 35, while the driving voltage V_{PZT} varies from 1 V to 5 V (corresponding values of D are 3.5 rad, 7 rad, 10.5 rad, 14 rad, and 17.5 rad, respectively). By comparing Figs. 6(a)–6(e), it can be seen that when the TSI is not used, the mismatch

between the demodulated phase and the original phase gets larger with an increase in V_{PZT}, indicating a generation of phase distortion. However, when the TSI is applied, a good recovery of the vibration signals with V_{PZT} ranging from 1 V to 5 V is achieved. Figure 6(f) shows the amplitudes of the demodulated phase extracted at various V_{PZT} without and with the TSI, and the theoretical voltage-amplitude (V_{PZT}-D) response curve. The determination coefficient (R^2) between a series of the demodulated and theoretical phase amplitudes is only 0.265 6 when the TSI is not used, whereas this value increases to 0.990 6 for the case with the TSI. These results indicate that the TSI enhances the amplitude response performance of the DCM algorithm. It is noticed that, some wrapped phases are observed even with the TSI applied at V_{PZT}=5 V, as seen in Fig. 6(e) at 0.005 s and 0.015 s. This behavior can be attributed to the fluctuation of the voltage-amplitude response coefficient of the system.

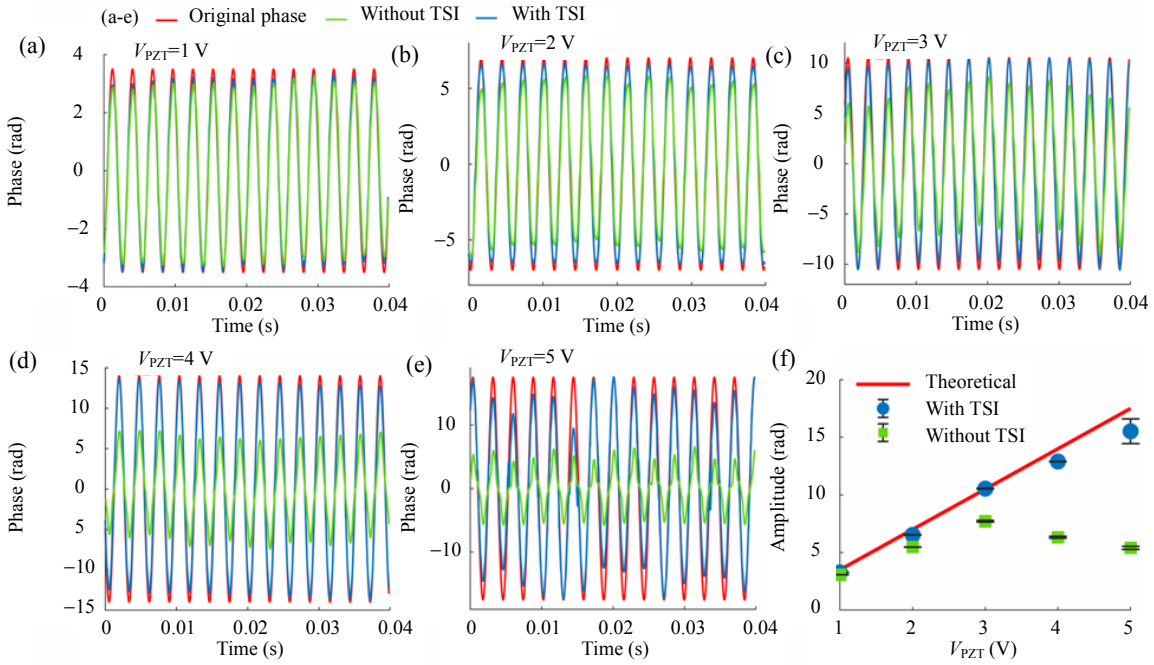

Fig. 6 Comparison of the time-domain waveforms of the demodulated phase without and with the TSI at different V_{PZT}: (a) 1 V, (b) 2 V, (c) 3 V, (d) 4 V, (e) 5 V, and (f) voltage-amplitude response curves without and with the TSI.

The RMSE distributions for the demodulated phase obtained at different values of f and D are utilized to analyze the amplitude-frequency response range. The RMSE distributions without and with the TSI are illustrated in Figs. 7(a) and 7(b), respectively. The horizontal and vertical axes represent the variations of the vibration frequency f and vibration amplitude D, respectively. The color ranging from bright yellow to dark blue indicates an increase in the RMSE value from 0 to 1, reflecting changes in phase distortion. In the experiment, the vibration frequencies f are set to 357 Hz, 417 Hz, 500 Hz, 625 Hz, 834 Hz, 1 250 Hz, and 1 563 Hz, respectively, corresponding to ratios f_{pulse}/f of 35, 30, 25, 20, 15, 10, and 8. The amplitudes D vary from 0.7 rad to 17.5 rad, with a step of 0.35 rad. A comparison between Figs. 7(a) and 7(b) clearly shows that, when the TSI is used, the RMSEs of the demodulated phase are reduced. This reduction becomes more prominent with an increase in f or D. The contour lines at RMSE=0.1 indicate that the TSI expands the amplitude-frequency response range of the DCM algorithm. The above improvements can be explained as follows: the TSI method interpolates the signal $I_m(t_s)$, effectively "increasing" f_{pulse} from a data processing perspective and "narrowing down"

Δt_s, thereby establishing a heightened level of precision for demodulating vibration signals with the larger D and f.

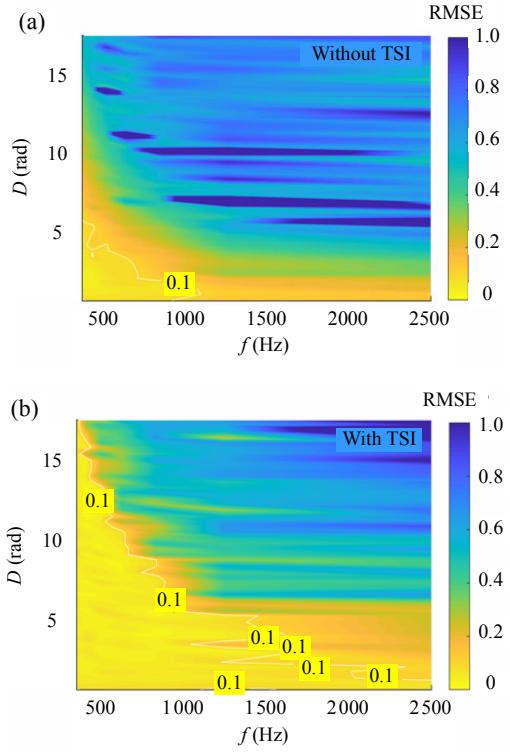

Fig. 7 Comparison of amplitude-frequency response ranges between the cases (a) without the TSI and (b) with the TSI.

We consider that a responsive vibration signal should satisfy that the RMSE of the demodulated phase is within 0.1, and its amplitude and frequency are defined as the responsive parameters. According to the amplitude-frequency response characteristic of the DCM algorithm, there exists a relationship among the parameters f_{pulse}, f, and D [30]:

$$n_D(D+1)f \le f_{\text{pulse}} \tag{5}$$

where n_D represents the minimum number to sample the maximum frequency component $(D+1)f$ of the signal $I_m(t_s)$, and its value can be determined by fitting a series of amplitude-frequency response points under a certain RMSE tolerance. The values of n_D are different for the cases without and with the TSI, owing to their different values of amplitude-frequency response points.

To obtain the values of n_D for the cases without and with the TSI, the maximum responsive vibration amplitude $D_{\max}$ is extracted at different ratios f_{pulse}/f when RMSE tolerance is 0.1. These amplitudes $D_{\max}$ are plotted as a bar graph, as shown in Fig. 8. It can be observed that with the TSI, the $D_{\max}$ values are higher than those without the TSI, and the $D_{\max}$ increases with the f_{pulse}/f. The fitting results of these amplitude-frequency response points using (5) indicate that without the TSI, the value of n_D is 5.3, while with the TSI, the value of n_D is 1.9. A smaller value of n_D implies a wider amplitude-frequency response range of the system. Therefore, the amplitude-frequency response characteristic is significantly enlarged by using the TSI compared to the case without the TSI, and it satisfies the expression $1.9(D+1)f \le f_{\text{pulse}}$. In the experiment, the demodulated cutoff frequency can reach 1462 Hz for vibration signals with the amplitude D of 3.5 rad.

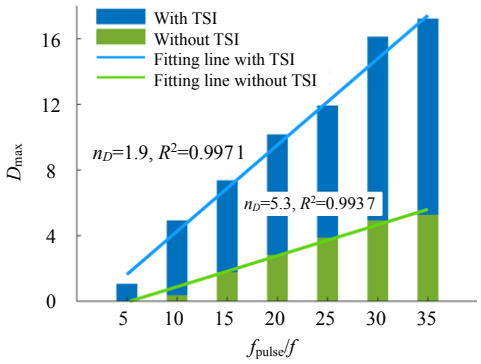

Fig. 8 Response relationship between f_{pulse}/f and $D_{\max}$ for the DCM algorithm without or with the TSI under RMSE tolerance being 0.1.

It is worth noting that for vibration signals with the given frequency f and amplitude D, when the f_{pulse} is greater than $5.3(D+1)f$, the RMSEs of demodulated phases are within 0.1 for both cases without and with the TSI, indicating that the improvement effect of the TSI on the phase demodulation quality is not significant. However, with a decrease in the f_{pulse} till $1.9(D+1)f$, the RMSEs of the demodulated phase without the TSI gradually increase, while with the TSI, the RMSEs remain below 0.1, indicating that the improvement effect of the TSI on the phase demodulation quality

is the best under this condition. This is because the TSI "narrows" the value of Δt_s, decreases the differential approximation errors, and thus reduces the phase errors, particularly at lower f_{pulse}. Therefore, in practical applications, the TSI can better improve the performance of the DCM algorithm for scenarios that require a wide range of amplitude-frequency responses in long-distance sensing. In addition, although the noise immunity of the DCM algorithm can be improved by the use of the TSI, phase distortion can still be caused when the system is under high levels of noise. Filtering or denoising processing can be employed to reduce the noise level present in the raw data.

4. Conclusions

In summary, this paper introduces a TSI pre-processing method to enhance the phase demodulation performance of the DCM algorithm. By performing nonlinear fitting and interpolation on the temporal signals characterizing RBS traces, the sampling time interval Δt_s is "narrowed", effectively reducing the differential approximation errors. This refinement leads to a heightened precision in phase demodulation. The improvement capability of the TSI to the DCM algorithm has been confirmed by experiments. The comparative results obtained without and with the TSI indicated that, when the TSI is applied, the DCM algorithm achieves better phase demodulation quality and the low-frequency noise components are suppressed. In addition, the amplitude-frequency response characteristic is studied by varying the amplitude and frequency ranges of the vibration signal. The results showed that when the RMSE tolerance is 0.1, the amplitude-frequency response range of the DCM algorithm with the TSI is enlarged and its characteristic can be expressed as $1.9(D+1)f \le f_{\text{pulse}}$. The proposed TSI has the potential for being applied in long-distance fiber sensing.

Acknowledgment

This work was supported in part by the National Natural Science Foundation of China (Grant Nos. 62075153, 62075151, and 62205237); in part by the Shanxi Provincial Key Research and Development Project (Grant No. 202102150101004); in part by the Shanxi Provincial Central Guiding Local Science and Technology Development Fund Project (Grant No. YDZJSX20231A019); in part by National Key Research and Development Program of China (Grant No. 2023YFF0715700); in part by Natural Science Foundation for Young Scientists of Shanxi Province (Grant No. 20210302124396).

Declarations

Conflict of Interest The authors declare that they have no competing interests.

References

[1] J. B. Ajo-Franklin, S. Dou, N. J. Lindsey, I. Monga, C. tracy, M. Robertson, *et al.*, "Distributed acoustic sensing using dark fiber for near-surface characterization and broadband seismic event detection," *Scientific Reports*, 2019, 9(1): 1–14.

[2] N. J. Lindsey, T. C. Dawe, and J. B. Ajo-Franklin, "Illuminating seafloor faults and ocean dynamics with dark fiber distributed acoustic sensing," *Science*, 2019, 366(6469): 1103–1107.

[3] A. Bakulin, I. Silvestrov, and R. Pevzner, "Surface seismics with DAS: an emerging alternative to modern point-sensor acquisition," *Leading Edge*, 2020, 39(11): 808–818.

[4] D. Milne, A. Masoudi, E. Ferro, G. Watson, and L. Le Pen, "An analysis of railway track behavior

based on distributed optical fibre acoustic sensing," *Mechanical Systems and Signal Processing*, 2020, 142: 106769.

[5] J. Tejedor, J. MacIas-Guarasa, H. F. Martins, S. Martin-Lopez, and M. Gonzalez-Herraez, "A contextual GMM-HMM smart fiber optic surveillance system for pipeline integrity threat detection," *Journal of Lightwave Technology*, 2019, 37(18): 4514–4522.

[6] A. H. Hartog, "*An introduction to distributed Optical fibre sensors*," London: Taylor & Francis Group, 2017: 239–241.

[7] Z. Pan, K. Liang, Q. Ye, H. Cai, R. Qu, and Z. Fang, "Phase-sensitive OTDR system based on digital coherent detection," in *2011 Asia Communications & Photonics Conference & Exhibition*, Shanghai, China, 2011, pp. 1–6.

[8] Z. Wang, L. Zhang, S. Wang, N. Xue, F. Peng, M. Fan, *et al.*, "Coherent Φ-OTDR based on *I*/*Q* demodulation and homodyne detection," *Optics Express*, 2016, 24(2): 853–858.

[9] D. Chen, Q. Liu, X. Fan, and Z. He, "Distributed fiber-optic acoustic sensor with enhanced response bandwidth and high signal-to-noise ratio," *Journal of Lightwave Technology*, 2017, 35(10): 2037–2043.

[10] Y. Shang, Y. Yang, C. Wang, X. Liu, C. Wang, and G. Peng, "Optical fiber distributed acoustic sensing based on the self-interference of Rayleigh backscattering," *Measurement*, 2016, 79: 222–227.

[11] G. Fang, T. Xu, S. Feng, and F. Li, "Phase-sensitive optical time domain reflectometer based on phase-generated carrier algorithm," *Journal of Lightwave Technology*, 2015, 33(13): 2811–2816.

[12] X. Lu, M. A. Soto, P. J. Thomas, and E. Kolltveit, "Evaluating phase errors in phase-sensitive optical time-domain reflectometry based on *I*/*Q* demodulation," *Journal of Lightwave Technology*, 2020, 38(15): 4133–4141.

[13] A. Masoudi and T. P. Newson, "Analysis of distributed optical fibre acoustic sensors through numerical modelling," *Optics Express*, 2017, 25(25): 32021–32040.

[14] M. Chen, A. Masoudi, and G. Brambilla, "Performance analysis of distributed optical fiber acoustic sensors based on φ-OTDR," *Optics Express*, 2019, 27(7): 9684–9695.

[15] A. Masoudi, M. Belal, and T. P. Newson, "A distributed optical fibre dynamic strain sensor based on phase-OTDR," *Measurement Science and Technol*ogy, 2013, 24(8): 085204.

[16] C. Wang, Y. Shang, W. A. Zhao, X. H. Liu, C. Wang, G. D. Peng, "Investigation and comparison of φ-OTDR and OTDR-interferometry via phase demodulation," *IEEE Sensors Journal*, 2018, 18(4): 1501–1505.

[17] C. Wang, Y. Shang, X. H. Liu, C. Wang, H. H. Yu, D. S. Jiang, *et al.*, "Distributed OTDR-interferometric sensing network with identical ultra-weak fiber Bragg gratings," *Optics Express*, 2015, 23(22): 29038–29046.

[18] C. Wang, Y. Shang, X. H. Liu, C. Wang, H. Z. Wang, and G. D. Peng, "Interferometric distributed sensing system with phase optical time-domain reflectometry," *Photonic Sensors*, 2017, 7(2): 157–162.

[19] C. Wang, C. Wang, Y. Shang, X. H. Liu, and G. D. Peng, "Distributed acoustic mapping based on interferometry of phase optical time-domain reflectometry," *Optics Communications*, 2015, 346: 172–177.

[20] V. Türker, F. Uyar, T. Kartaloğlu, E. Özbay, and İ. Özdür, "Long-range distributed acoustic sensor based on 3×3 coupler assisted passive demodulation Scheme," in *2022 Conference on Lasers and Electro-Optics*, San Jose, USA, 2022, pp. 1–2.

[21] W. Li and J. Zhang, "Distributed weak fiber Bragg grating vibration sensing system based on 3×3 fiber coupler," *Photonic Sensors*, 2018, 8(2): 146–156.

[22] X. Zhong, D. Gui, B. Zhang, H. Deng, S. Zhao, J. Zhang, M. Ma, and M. Xu, "Performance enhancement of phase-demodulation ϕ-OTDR using improved two-path DCM algorithm," *Optics Communications*, 2021, 482: 126616.

[23] Z. Peng, J. Jian, H. Wen, A. Gribok, M. Wang, H. Liu, *et al.*, "Distributed fiber sensor and machine learning data analytics for pipeline protection against extrinsic intrusions and intrinsic corrosions," *Optics Express*, 2020, 28(19): 27277–27292.

[24] Z. Peng, H. Wen, J. Jian, A. Gribok, M. Wang, S. Huang, *et al.*, "Identifications and classifications of human locomotion using Rayleigh-enhanced distributed fiber acoustic sensors with deep neural networks," *Scientific Reports*, 2020, 10(1): 1–11.

[25] Y. Shang, Q. He, S. Huang, J. Wang, M. Wang, D. Li, *et al.*, "Inversion method for soil moisture content based on a distributed fiber optic acoustic sensing system," *Optical Express*, 2023, 31(23): 38878–38890.

[26] W. Fu, D. Yi, Z. Huang, C. Huang, Y. Geng, and X. Li, "Multiple event recognition scheme using variational mode decomposition-based hybrid feature extraction in fiber optic DAS system," *IEEE Sensors Journal*, 2023, 23(22): 27316–27323.

[27] X. Wang, C. Wang, F. Zhang, S. Jiang, Z. Sun, H. Zhang, *et al.*, "Feature fusion-based fiber-optic distributed acoustic sensing signal identification method," *Measurement Science and Technology*, 2023, 34(12): 125141.

[28] X. Lu and P. J. Thomas, "Phase error evaluation via differentiation and cross-multiplication demodulation in phase-sensitive optical time-domain reflectometry," *Photonics*, 2023, 10(5): 514.

[29] Y. Muanenda, S. Faralli, C. J. Oton, C. Cheng,

M. Yang, and F. Di Pasquale, "Dynamic phase extraction in high-SNR DAS based on UWFBGs without phase unwrapping using scalable homodyne demodulation in direct detection," *Optics Express*, 2019, 27(8): 10644–10658.

[30] T. Wang, J. Zhang, Z. Ma, M. Liu, X. He, W. Li, *et al.*, "Comparison of amplitude-frequency response characteristics between DCM and Arctan algorithms in ϕ-OTDR," *Journal of Lightwave Technology*, 2023, 41(20): 6608–6614.

[31] P. C. Hammer, "Finite-difference methods for partial differential equations," *Technometrics*, 1962, 4(1): 143–144.

[32] L. László, "Cubic spline interpolation with quasiminimal B-spline coefficients," *Acta Mathematic Hungarica*, 2005, 107: 77–87.

[33] H. S. Hou and H. C. Andrews, "Cubic splines for image interpolation and digital filtering," *IEEE Transactions on Acoustics Speech and Signal Processing*, 1978, 26(6): 508–517.